RSC Advances

PAPER

View Article Online
View Journal | View Issue

Cite this: *RSC Adv.*, 2026, **16**, 19687

High-efficiency electro-Fenton mineralization of triclosan using a novel octahedral iron(III) complex: structure, mechanism, and performance

Nejmeddine Rabaaoui,[a] Ahlem Guesmi,[b] Wiem Jabeur,[a] Noureddine Mhadhbi,[ae] Naoufel Ben Hamadi,[b] Lotfi Khezami,[b] Mourad Cherif[cd] and Houcine Naïli *[a]

Received 19th February 2026
Accepted 7th April 2026

DOI: 10.1039/d6ra01483f

rsc.li/rsc-advances

This study reports the synthesis and structural elucidation of a novel iron(III) coordination complex, $[Fe(CO_3)(en)_2]Cl$ (1), and its integration as an efficient cathodic modifier in an advanced electro-Fenton (EF) system for the degradation of the emerging pollutant triclosan. Unlike conventional EF systems, the rationally designed iron complex enhances iron redox cycling and hydroxyl radical generation, leading to significantly improved mineralization efficiency. Under optimized conditions, the modified system achieved over 97% TOC removal within 210 min, following pseudo-first-order kinetics (k = 0.0195 min^{-1}). Mechanistic investigations revealed progressive dechlorination and oxidation into short-chain carboxylic acids prior to complete mineralization. This work demonstrates how coordination chemistry can be strategically integrated into electrochemical advanced oxidation processes to improve efficiency, stability, and sustainability in wastewater treatment applications.

1 Introduction

In recent years, the rational design and synthesis of coordination compounds have garnered significant interest. This attention arises not only from the compelling structural characteristics of these complexes, but also from their promising potential applications across various scientific disciplines.[1–8] There are many prospects for clean technologies and sustainable development in the dynamic area of photocatalysis research. Semiconductors have showcased great promise in environmental remediation and photocatalytic energy generation, serving as efficient materials for harnessing light energy to drive chemical transformations. Building on this foundation, recent research has witnessed a significant renaissance in developing high-performance photocatalysts made from earth-abundant transition metals.[9,10] These include iron,[11–13] copper,[14,15] cobalt,[16] molybdenum, [17] nickel,[18] tungsten,[19,20] and zirconium.[21] Beyond photocatalytic applications, these transition metal complexes have enabled many novel transformations, acting as highly effective photocatalysts. With their visible light photoactivity, iron species have significant potential as energy-efficient photocatalysts for degrading toxic and persistent organic pollutants. Moreover, they are non-toxic, affordable, and abundantly available. Iron, which constitutes approximately 5.0% of the Earth's crust, ranks as the second most abundant metal globally. It has been widely employed in photocatalytic applications to enhance charge carriers' generation, separation, and efficiency. Owing to its natural abundance, environmental compatibility, and notable photocatalytic properties, iron-based catalysts have emerged as promising materials in this field.[22–24] Recent advances in electrochemical advanced oxidation processes have emphasized that catalytic performance is not solely governed by the presence of active metal species but is strongly influenced by the electronic structure of catalytic centers. In particular, the modulation of electron density and coordination environment has emerged as a key strategy to enhance redox activity, control reactive oxygen species (ROS) generation, and improve overall catalytic efficiency. For instance, electron-deficient metal centers have been shown to promote enhanced oxidative pathways, as demonstrated in Co(III)-based systems where tailored electronic configurations significantly improved electrochlorination efficiency and ammonia removal.[25] Similarly, recent studies on single-atom catalysts have revealed that fine-tuning the electronic structure of isolated active sites can enable the selective *in situ* generation of specific ROS, such as singlet oxygen ($^1O_2$), thereby opening new avenues for controlled electro-Fenton processes.[26]

[a]*Laboratory Physical-Chemistry of the Solid State, Department of Chemistry, Faculty of Sciences of Sfax, University of Sfax, B.P. 1171, Sfax 3000, Tunisia. E-mail: houcine_naili@yahoo.com*

[b]*Chemistry Department, College of Science, Imam Mohammad Ibn Saud Islamic University (IMSIU), P.O. Box 5701, Riyadh 11432, Saudi Arabia*

[c]*Laboratoire de Physico-Chimie des Matériaux, IPEST, BP51, 2070 La MARSA, Tunisia*

[d]*IPEIEM, Université de Tunis-El Manar, BP244, 2096, El Manar II, Tunisia*

[e]*University of Monastir, Preparatory Institute for Engineering Studies of Monastir, 5019 Monastir, Tunisia*

Triclosan (TCS), chemically defined as 5-chloro-2-(2,4-dichlorophenoxy) phenol ($C_{12}H_7Cl_3O_2$), is a synthetic antimicrobial agent widely incorporated into personal hygiene and consumer products such as soaps, toothpastes, shampoos, and deodorants.[27] Its hydrophobic nature, reflected by a high octanol–water partition coefficient, facilitates pronounced bioaccumulation in aquatic organisms, raising significant ecological and toxicological concerns.[28] Although partially removed during conventional wastewater treatment, substantial concentrations of TCS persist in treated effluents, contributing to its frequent detection in surface waters.[29] Moreover, its chemical stability across a broad pH range and resistance to biodegradation complicates its elimination.[30,31] Long-term environmental exposure has been associated with endocrine disruption, neurotoxicity, and developmental toxicity, particularly in aquatic species.[32] Under ultraviolet radiation, TCS may transform into highly toxic polychlorinated dioxins, exacerbating its environmental risk.[33] Its presence in human biological fluids—such as blood, urine, and breast milk—further underscores its physiological relevance, highlights the scope of chronic exposure, and the pressing need for advanced and sustainable remediation technologies.[34]

Over the past decade, various treatment strategies have been employed for TCS removal, including chlorination, ozonation, adsorption, photocatalysis, and biological degradation.[34–36] However, each approach is hindered by inherent limitations: chlorination may generate harmful halogenated by-products;[37] ozonation often results in incomplete mineralization;[38] adsorption merely transfers the pollutant to a secondary solid phase;[39] and biodegradation remains largely ineffective due to the recalcitrant nature of TCS.[40] In contrast, advanced oxidation processes, particularly those based on Fenton chemistry, have shown high potential due to their generation of highly reactive hydroxyl radicals, which can non-selectively oxidize a broad spectrum of organic pollutants. Nevertheless, classical Fenton systems suffer from operational challenges, such as the requirement for acidic conditions, iron sludge generation, and limited control over radical production.[41]

Electrochemical advanced oxidation processes, notably the electro-Fenton technique, have emerged as promising alternatives due to their controllability and efficiency.[42] EF systems operate through the *in situ* electrochemical generation of hydrogen peroxide at the cathode and subsequent Fenton-like reactions catalyzed by Fe^{3+}, enabling both homogeneous and heterogeneous oxidation pathways. When coupled with high-performance anodes such as boron-doped diamond, these systems also facilitate direct anodic oxidation *via* surface-generated $^{\bullet}OH$ radicals.[40] The overall effectiveness of EF systems, however, is closely tied to the nature of the electrode materials-particularly the cathode-which governs the kinetics of H_2O_2 production and iron redox cycling.[43] Despite these significant advances, most reported systems rely on complex material architectures, such as single-atom catalysts or electronically engineered heterogeneous materials, which may suffer from limited structural definition, synthetic complexity, or challenges in correlating catalytic performance with well-defined active sites. In contrast, the use of structurally well-defined coordination compounds as tunable platforms for modulating electronic properties in electrochemical systems remains relatively underexplored. In particular, the integration of molecularly defined iron coordination complexes into electro-Fenton systems offers a promising alternative approach, where the coordination environment can be precisely controlled to influence redox behavior, interfacial electron transfer, and catalytic stability. However, the extent to which such systems contribute to the interplay between homogeneous and interfacial catalytic pathways is still not fully understood and warrants further investigation.

In response to this, the present study introduces a novel iron(III) complex, $[Fe(CO_3)(en)_2]Cl$, as a cathodic modifier within an EF framework. The compound utilizes ethylenediamine (en), a widely studied bidentate ligand, to form stable five-membered chelate rings that enhance coordination stability and redox behavior. The iron center exhibits an octahedral geometry coordinated by two en ligands and one coordinated carbonate group, establishing a structurally robust and redox-active platform. The solution and electron-donating properties of en further contribute to favorable interfacial behavior and electrochemical performance. Before being employed in electrochemical studies, the complex was synthesized and comprehensively characterized using single-crystal X-ray diffraction, FT-IR, Raman spectroscopy, and thermal analysis, which verified its structural stability and physicochemical robustness. Accordingly, this research seeks to bridge molecular design with environmental functionality by integrating the synthesized complex into an optimized electro-Fenton system for the degradation of triclosan. The study evaluates its catalytic performance, investigates the evolution of degradation intermediates, and proposes a mechanistic pathway toward full mineralization. This integrated approach illustrates the potential of rationally engineered coordination compounds to enhance next-generation water treatment systems' selectivity, efficiency, and sustainability.

2 Materials and methods

2.1. Synthesis of $[Fe(CO_3)(en)_2]Cl$

Ethylenediamine monohydrochloride (0.19312 g, 2 mmol) was first dissolved in 10 mL of absolute ethanol. This ethanolic solution was then combined with a 10 mL aqueous solution containing iron(II) carbonate ($FeCO_3$) (0.11585 g, 1 mmol). The resulting mixture was refluxed for approximately 2 hours. Following filtration and gradual cooling, the solution was allowed to stand at room temperature under ambient conditions until most of the solvent evaporated. A colorless, block-shaped crystalline product of compound 1 was obtained and subsequently dried in a desiccator. Yield: 78.7%. Anal. Calc. For $C_5H_{16}N_4O_3ClFe$ (M_r = 271.52): C, 61.16; H, 6.02; N, 11.44. Found: C, 62.95; H, 6.24; N, 11.09%. FTIR (ATR, cm^{-1}): 3462, 2982, 2724, 1534, 1561, 1020, 536.

2.2. Characterization techniques

2.2.1. Single-crystal X-ray structural analysis. X-ray diffraction measurements for compound 1 were carried out at 100 K

using a XtaLAB Synergy Dualflex diffractometer equipped with a HyPix-Arc 100 detector and a Triumph curved graphite monochromator paired with a Mo Kα fine-focus sealed X-ray tube. The processes of data collection, cell refinement, and data reduction were conducted using Olex2 version 1.5-ac5-024.[44] The crystal structure was solved *via* ShelXT 2018/2,[45] and intensity-based refinement was performed with SHELXL-2018/3.[46] Structural representations were created using the Diamond software package.[47] Table 1 provides detailed crystallographic data and experimental conditions for the crystal structure. Complete crystal data, collection, and refinement parameters for this compound have been deposited with the Cambridge Crystallographic Data Centre under the supplementary publication number CCDC 2446786. Copies of these data can be obtained at no cost by contacting the CCDC, 12 Union Road, Cambridge, CB2 1EZ, UK (Fax: +44 1223 336408 or email: https://www.ccdc.cam.ac.uk/deposit/).

2.2.2. Spectroscopic measurements. The FT-IR spectrum was acquired using a PerkinElmer 400 spectrometer, operating within a frequency range of 450 to 4000 cm^{-1} and employing the UATR technique.

The Raman measurements were obtained using a Fisher DXR Raman Thermo-spectrometer, employing the Raman spectroscopy technique under experimental conditions including a 532 nm laser wavelength, 10 mW laser power, and a spectral range spanning 50 to 3500 cm^{-1}.

2.2.3. Thermal analysis. TGA measurements were performed with Jade TGA (Thermogravimetric Analyzer, Pyris 6 TGA, PerkinElmer). DSC analyses were conducted on a Jade DSC device under a nitrogen environment, applying a heating rate of 10 °C per minute. Measurements were taken across a temperature range from 25 to 400 °C.

2.3. Application in triclosan herbicide degradation

2.3.1. Electrodes preparation. Boron-doped diamond (BDD) films were supplied by CSEM and grown on conductive p-type silicon substrates (1 mm thick, Siltronix) using a hot filament chemical vapor deposition (HF-CVD) technique. The filament temperature ranged between 2440 and 2560 °C, while the substrate temperature was controlled at approximately 830 °C. The reactive gas mixture consisted of 1% methane in hydrogen, doped with 1–3 ppm of trimethyl boron. This gas blend was introduced into the reaction chamber at a flow rate of 5 L min^{-1}, resulting in a diamond growth rate of 0.24 μm h^{-1}. The process yielded a columnar, randomly oriented polycrystalline diamond film with a thickness near 1 μm and a resistivity of 15 mΩ cm (±30%) deposited on the conductive p-Si substrate.[48,49]

A glassy carbon electrode (GCE) with a diameter of 3 mm served as the cathode substrate. The glassy carbon electrode (GCE) was selected as cathodic substrate due to its high electrical conductivity, chemical inertness, wide electrochemical potential window, and excellent surface stability under acidic electro-Fenton conditions. Moreover, its smooth and reproducible surface facilitates uniform catalyst film deposition and enhances electron transfer kinetics, promoting efficient H_2O_2 electrogeneration and Fe^{3+}/Fe^{2+} redox cycling. Before modification, the electrode surface was polished sequentially using a 0.05 μm alumina slurry, followed by thorough rinsing with deionized water and ethanol, then dried under a nitrogen stream. To prepare the catalyst ink, 5 mg of the synthesized $[Fe(CO_3)(en)_2]Cl$ complex was ultrasonically dispersed in a solvent mixture consisting of 450 μL ethanol, 450 μL deionized water, and 100 μL of 5 wt% Nafion®. The resulting suspension was sonicated for 30 minutes to achieve uniform dispersion. Subsequently, 7 μL of this ink was drop-cast onto the GCE surface and dried at 60 °C for 30 minutes, forming a consistent catalytic layer. The modified electrode was then stored in a desiccator until further use.

2.3.2. Reagents and electrolytes. Sodium sulfate (Na_2SO_4, ACS reagent, ≥99.0%), triclosan (99.8%), sodium chloride (NaCl, ≥99.5%), sodium hydroxide (NaOH, ≥98.0%), and methanol (CH_3OH, ≥99.9%) were obtained from Sigma-Aldrich and used directly without further purification. All aqueous solutions were prepared using deionized water from a Millipore Milli-Q system, with a resistivity exceeding 18 MΩ cm. 2,4-dichlorophenol, 2,4,6-tichlorophenol, 4-chlorocatechol, 1,2,4-trihydroxybenzene, oxalic acid, acetic acid, succinic acid, and formic acid were of analytical grade and purchased from Sigma-Aldrich. They were utilized to identify by-products formed during the degradation of triclosan.

2.3.3. Electro-Fenton galvanostatic degradation of triclosan. Electro-Fenton experiments were carried out at ambient temperature (25 ± 2 °C) in a 250 mL single-compartment glass cell equipped with continuous magnetic stirring and aeration. The electrolysis was performed under galvanostatic mode using a two-electrode setup, powered by a regulated direct current (DC) power source. A boron-doped diamond plate (2.5 × 4 cm^2) was used as the anode, with the cathode composed of a glassy carbon electrode (GCE, 3 mm diameter) coated with a thin layer of the synthesized hybrid perovskite $[Fe(CO_3)(en)_2]Cl$. The supporting electrolyte consisted of 50 mmol L^{-1} Na_2SO_4, and Fe^{2+} ions (0.2 mmol L^{-1} as $FeSO_4 \cdot 7H_2O$) were added to initiate the Fenton reaction. The addition of Fe^{2+} (0.2 mmol L^{-1} as $FeSO_4 \cdot 7H_2O$) was employed to ensure efficient initiation of the Fenton reaction, as commonly adopted in electro-Fenton systems. It is important to note that the present system is designed to operate through a hybrid mechanism involving both homogeneous iron species in solution and interfacial catalytic processes at the modified cathode. In this context, the $[Fe(CO_3)(en)_2]Cl$ complex is not intended to act as the primary source of dissolved iron, but rather as a cathodic modifier that enhances interfacial electron transfer, facilitates the Fe^{3+}/Fe^{2+} redox cycle at the electrode surface, and contributes to improved H_2O_2 electrogeneration. The initial triclosan concentration was set at 30 mg L^{-1}, and the solution pH was adjusted to 3.0 using diluted H_2SO_4. The distance between the electrodes was maintained at approximately 2 cm. A constant galvanostatic current density of 20 mA cm^{-2} was applied during the electro-Fenton process to maintain steady-state conditions for evaluating degradation kinetics and mineralization efficiency. Throughout the reaction, both voltage and current were continuously recorded with a digital multimeter. Samples (2 mL) were collected at predetermined intervals (0, 15, 30, 60, 90, 120, 150,

and 180 minutes), filtered through 0.22 μm membrane filters, and promptly analyzed.

2.3.4. Analytical measurements. All solutions were prep ared using distilled water, and the temperature was controlled by a thermostatic water bath. Current density measurements were conducted with a Bench Power Supply GPC-3030D potentiostat–galvanostat. Chemical oxygen demand (COD) was determined using a Beckman UV/Vis DU 800 spectrophotometer. Total organic carbon (TOC) content was measured with a Shimadzu VCSH TOC analyzer. For TOC analysis, samples were filtered through a 0.45 μm Millipore syringe filter, and 50 μL aliquots were injected into the analyzer. The concentrations of triclosan and its reaction intermediates were quantified using a Spectra SYSTEM HPLC (Thermo Fisher Scientific) equipped with a diode array detector (DAD). Separation was performed on a ZORBAX Eclipse XDB-C18 reverse-phase column (150 mm × 4.6 mm, 5 μm particle size). HPLC analysis involved injecting 20 μL aliquots, using a mobile phase composed of water and methanol (70 : 30 v/v) at a flow rate of 0.8 mL min^{-1} in isocratic mode. For kinetic measurements, detection was carried out at 230 nm.

3 Results and discussion

3.1. Characterization of $[Fe(CO_3)(en)_2]Cl$

3.1.1. Crystal structure description. Compound 1 crystallizes in the orthorhombic crystal system, adopting the $Pca2_1$ space group. The asymmetric unit, illustrated in Fig. 1, contains a mononuclear $[Fe(CO_3)(en)_2]^+$ coordination cation and a chloride anion Cl^-. The complex cation comprises two *N*,*N*′-chelating ethylenediamine ligands and one *O*,*O*′-chelating carbonate ligand. The carbonate ligand chelates the iron center, with its two oxygen atoms occupying adjacent (*cis*) coordination sites. Bite angles from chelation (O–Fe–O ≈ 69°, N–Fe–N ≈ 86°) introduce strain, while trans angles deviate from 180° (≈166–177°), leading to a distorted octahedral geometry.

The Fe^{3+} center exhibits a markedly distorted octahedral FeN_4O_2 coordination sphere, bound to four nitrogen atoms from two bidentate ethylenediamine ligands and two oxygen atoms from a single *O*,*O*′-chelating carbonate (CO_3^{2-}) group occupying adjacent cis sites (Fig. 1b). Each ethylenediamine ligand forms a five-membered N–N–Fe–N–N chelate ring with a bite angle of approximately 86°. In contrast, the O–Fe–O bite is strongly compressed to about 69°, a consequence of the rigid trigonal-planar geometry of the coordinated carbonate, which imposes pronounced angular strain. As a result, trans angles such as N2–Fe–N3 and mixed O–Fe–N (N4–Fe–O1) orientations deviate significantly from the ideal 180°, ranging between 166° and 178°. This distortion originates from steric competition between compact ethylenediamine ligands and the planar carbonate moiety, generating a puckered coordination environment intermediate between a distorted octahedron and a trigonal form. Structural analysis of the Fe(III) center using the octahedral distortion parameter Δ yields a value of 1.492×10^{-5} Å, indicating a very slightly distorted octahedral geometry (FeN_4O_2) consistent with well-refined Fe(III) analogues. This value was obtained using the following formula (eqn (1)):[50–52]

$$\Delta = \left(\frac{1}{N}\right)\sum\left(\frac{d_i - d_m}{d_m}\right)^2 \quad (1)$$

where $N = 6$ represents the total number of bonds, d_i denotes each individual bond distance, and d_m is the average bond distance within the octahedron.

The total angular deviation from ideal 90° cis angles (Σ = 107°) arise primarily from the sharply contracted O–Fe–O bite (~69°) and the slightly expanded N–Fe–N chelate angles (85.99(10)°–86.46(9)°), representing only a ~4° increase over the strain-free optimum (~82°) typical for ethylenediamine in six-coordinate environments.[53] Moreover, bond length analysis (Table 2) further supports this subtle distortion, where the Fe–O distances fall within a narrow range of 1.9107(18)–1.9257(18) Å, reflecting strong, symmetric σ-donation from the bidentate

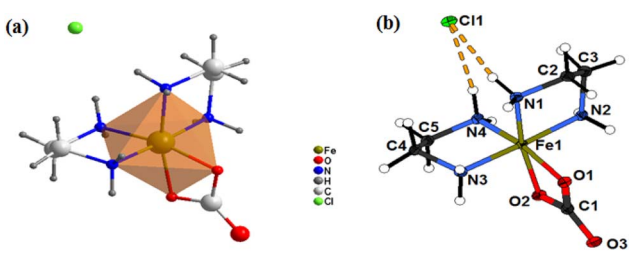

Fig. 1 (a) Coordination environment of the metal center and (b) ORTEP illustration of the asymmetric unit in the molecular structure of $[Fe(CO_3)(en)_2]Cl$. Hydrogen bonds are represented by dotted lines.

Table 1 Crystal data and refinement parameters for $[Fe(CO_3)(en)_2]Cl$

Crystal data	
Empirical formula	$C_5H_{16}FeN_4O_3Cl$
Color/form	Colourless/Block
Formula weight (g mol^{-1})	271.52
Volume ($Å^3$)	1007.29(5)
Calculated density (Mg m^{-3})	1.790
System	Orthorhombic
T (*K*)	100
Space group	$Pca2_1$
Z	4
a (Å), b (Å), c (Å)	10.7188(3), 11.0446(3), 8.5086(3)
Crystal size (mm)	0.12 × 0.10 × 0.06
Data collection	
Absorption correction	Multi-scan
T_{min} and T_{max}	0.862, 1.000
Index ranges	$-14 \le h \le 13$, $-13 \le k \le 15$, $-11 \le l \le 10$
Measured reflections	15 151
Independent reflections	2510
Reflections with $I > 2\sigma(I)$	2444
Refinement	
Number of parameters	128
$R_1[F^2 > 2\sigma(F^2)]$	0.0238
$wR_2(F^2)$	0.0580
GooF (S)	1.057

Table 2 Selected geometric parameters (Å, °) for $[Fe(CO_3)(en)_2]Cl$

Bond length (Å)					
Fe1–O1	1.9257(18)	Fe1–N1	1.963(2)	O1–C1	1.314(3)
Fe1–O2	1.9107(18)	Fe1–N2	1.953(2)	O2–C1	1.317(3)
Fe1–N3	1.954(2)	Fe1–N4	1.955(2)	O3–C1	1.245(3)
Fe1–C1	2.322(2)	N1–C2	1.485(4)	N2–C3	1.488(4)
N3–C4	1.485(4)	N4–C5	1.486(4)	C2–C3	1.511(4)
C4–C5	1.512(4)	N–H	0.9100	C–H	0.9900

Bond angle (°)					
O2–Fe1–O1	68.97(8)	O1–Fe1–N4	166.20(9)	O3–C1–O1	124.7(2)
O1–Fe1–N1	98.29(9)	O2–Fe1–N1	166.75(9)	O3–C1–O2	124.0(2)
O1–Fe1–N2	90.24(9)	O2–Fe1–N4	97.47(9)	O1–C1–O2	111.3(2)
O1–Fe1–N3	91.38(9)	N2–Fe1–N1	85.99(10)	C1–O1–Fe1	89.53(14)
N3–Fe1–N4	86.46(9)	N2–Fe1–N3	177.56(9)	C1–O2–Fe1	90.10(15)
N1–Fe1–N4	95.40(9)	N2–Fe1–N4	92.39(9)	O1–C1–Fe1	56.02(11)
N1–Fe1–N3	91.97(9)	C2–N1–Fe1	107.03(17)	O2–C1–Fe1	55.36(12)
C3–N2–Fe1	109.28(17)	C4–N3–Fe1	108.62(18)	C5–N4–Fe1	108.65(16)

Torsion angle (°)	
Fe1–O1–C1–O2	−2.7(2)
Fe1–O1–C1–O3	175.4(3)
Fe1–O2–C1–O1	2.7(2)
Fe1–O2–C1–O3	−175.4(3)
Fe1–N1–C2–C3	45.8(2)
Fe1–N2–C3–C2	37.9(3)
Fe1–N3–C4–C5	39.9(3)
Fe1–N4–C5–C4	39.1(2)
N1–C2–C3–N2	−54.7(3)
N3–C4–C5–N4	−51.7(3)

carbonate along with possible π-acceptor interactions. Corresponding Fe–N bonds span 1.953(2)–1.963(2) Å (average ≈ 1.956 Å), significantly shorter than the Fe–N(amine) length of 2.159(1) Å observed in the isonicotinato analogue $C_{28}H_{25}FeN_{12}O_4S_4$.[54] This contraction underscores the enhanced ligand field strength and compact coordination pocket imposed by the carbonate ethylenediamine assembly.

Regarding the other inorganic moiety present within the cation, the carbonate ligand adopts a trigonal planar geometry centered at C1 as labeled in Fig. 1a, with O1 and O2 symmetrically chelating Fe1 to form a strained four-membered Fe–O1–C1–O2 ring, while O3 (the tiled oxygen) remains non-coordinated and projects outward (Fig. 1); C1–O1 and C1–O2 bonds are slightly elongated (∼1.29–1.31 Å) due to coordination and ring strain, whereas the terminal C1–O3 bond is shorter (1.245(3) Å) indicating a strong π-character, reflecting greater double-bond character, with the O1–C1–O2 angle compressed to 111.3(2)° (ideal = 120°).[55] This ∼9° contraction is fully in-plane and arises from the geometric constraint of the κ^2-*O*,*O*′ chelation to Fe(III), which imposes an acute O–Fe–O bite angle of 68.97(8)°. The two flanking O–C–O angles are O3–C1–O1 = 124.7(2)° and O3–C1–O2 = 124.0(2)°, averaging 124.35(2)° to maintain planarity and charge delocalization. The entire CO_3 unit lies nearly coplanar, with the carbonate plane oriented approximately perpendicular to the mean plane of the two en chelate rings, minimizing steric repulsion, while O3 (as labeled in Fig. 1a) is poised for potential lattice hydrogen bonding. The planarity of the CO_3^{2-} group can be assessed by examining the deviations of its constituent atoms from the mean plane. This plane represents the best-fit surface that minimizes the overall displacement of the selected atoms typically the three oxygen atoms and the central carbon from an ideal flat geometry. The perpendicular distances of each atom from this plane are computed to quantify the planarity. In this structure, the carbonate group is essentially planar, exhibiting an RMSD of 0.0021 Å from the least-squares plane defined by the fractional coordinates, calculated using singular value decomposition.[56] This deviation confirming the absence of out-of-plane distortion, consistent with the sp^2 hybridization of the central carbon and the delocalized π-electron system over the three C–O bonds.

Furthermore, the chloride anion (Cl^-), labeled Cl1 (Fig. 1a), is positioned parallel to the *a*-axis. The Fe1···Cl1 separation of 4.356(1) Å unequivocally identifies chloride as a non-coordinating counteranion, located beyond the first coordination sphere of the $[FeCO_3(en)_2]^+$ cation. This distance is considerably longer than typical Fe–Cl bonding interactions and exceeds the sum of the van der Waals radii (Fe + Cl ≈ 3.8 Å), confirming the absence of any covalent interaction. The selected bond lengths and bond angles for compound 1 are summarized in Table 2.

In addition to the mineral constituents of the complex, the organic component plays a vital role in organizing the structure. The ethylenediamine (en) ligands in the distorted octahedral FeN_4O_2 complex, $[FeCO_3(en)_2]^+$, form two five-membered chelate rings (Fe–N–C–C–N) that adopt a puckered envelope (*δ*) conformation.[57,58] This is evidenced by the non-bonding N···N bite distances of 2.702(3) Å (N1···N2) and 2.709(3) Å (N3···N4), with an average of 2.705(3) Å. These separations correspond to C–C–N bond angles of 105.8(3)°–107.0(3)°, which are noticeably compressed relative to those in free ethylenediamine (≈112°)[59] and torsional preferences that minimize steric repulsion between methylene hydrogens. The degree of puckering is quantified by the torsion angles N1–C2–C3–N2 = 54.7(3)° and N3–C4–C5–N4 = 51.7(3)°, corresponding to *δ*(en) conformations,[58,59] with the C2–C3 and C4–C5 bonds serving as the flap atoms in the envelope.

This value is well-established from statistical analyses of $[M(en)_3]^{n+}$ structures,[60] where the mean N–M–N angle is 82.7 ± 1.5°. In the present $[FeCO_3(en)_2]^+$ cation, the observed N–Fe–N bite angles of ≈86° represent a modest ∼4° expansion from this ideal, induced by the acutely compressed O–Fe–O carbonate bite angle (≈69°), which displaces the en nitrogens outward to alleviate steric and electronic repulsion within the coordination sphere.[55] This minor deviation confirms that the ethylenediamine ligands experience negligible chelate strain of geometric distortion accommodated by the rigid carbonate ligand.

Fig. 2 illustrates the unit cell of $[Fe(CO_3)(en)_2]Cl$ projected onto the *ab* and *ac* planes, revealing a highly symmetric and densely packed ionic lattice within the polar orthorhombic space group $Pca2_1$. The cations form zigzag chains extending along the *c*-direction, generating an infinite three-dimensional

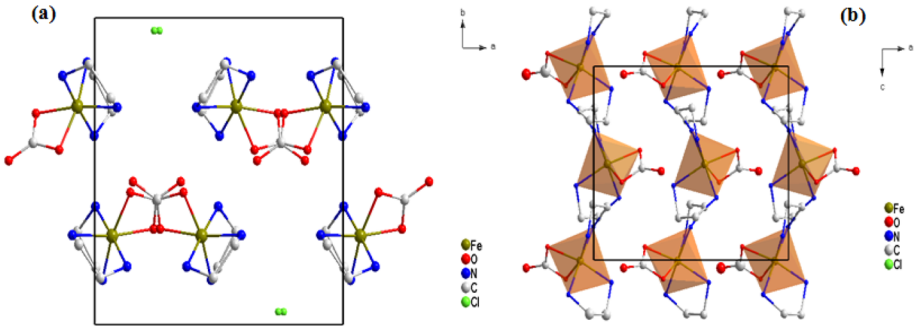

Fig. 2 (a) The unit cell of $[Fe(CO_3)(en)_2]Cl$ projected along the *c*-axis, showing two antagonistically oriented cationic double layers stacked along the *b*-direction (H atoms omitted for clarity). (b) Crystal structure of $[Fe(CO_3)(en)_2]Cl$ viewed along the *b*-axis, highlighting the distorted FeN_4O_2 coordination environment (H and Cl atoms omitted for better visualization).

ionic framework through periodic translation of the asymmetric unit along all three crystallographic axes (*a*, *b*, and *c*), with no connections of the FeN_4O_2 octahedra's. Within each double layer, the two cations are rotated by nearly 180° relative to each other, so that the carbonate O3 (titled O) atoms are oriented in opposite directions along both the *a*- and *c*-axes. This ABAB-type (A): oriented along –*a*; (B): along + *a*) stacking arrangement minimizes steric repulsion between ethylenediamine (en) and terminal carbonate oxygens, while chloride ions (Cl^-) occupy strategically positioned sites that reinforce the overall structural cohesion. The separation places Cl^- in the second coordination sphere, where it acts as a multidentate hydrogen-bond acceptor (N···Cl ≈ 3.274–3.382 Å) rather than as a ligand. The anion is surrounded by multiple N–H groups from the four ethylenediamine ligands, forming a robust network of N–H···Cl hydrogen bonds (H···Cl ≈ 2.38–2.53 Å).

This extensive hydrogen-bonding network stabilizes the ionic lattice, directs crystal packing along the polar *c*-axis in the $Pca2_1$ space group. This ABAB-type supramolecular assembly generates continuous channels within the *a*–*b* plane, where Cl^- ions maintain charge balance and contribute to the long-range structural order (Fig. 3).

Beyond these contacts, a complex hydrogen-bonding framework reinforces the overall cohesion and structural integrity of the crystal lattice. Each cation–anion pair is interconnected through an extensive array of hydrogen bonds, including, C–H···Cl, N–H···O, and C–H···O interactions, with H···A separations ranging from 1.97 to 2.94 Å. Together, these interactions form supramolecular linkages that consolidate the three-dimensional packing of the crystal. The geometric parameters of all hydrogen-bonding interactions in compound 1 are summarized in Table 3.

It is worth noting that the compound was obtained as a single phase, as shown in Fig. 4, given the excellent agreement between the experimental powder XRD pattern and the simulated pattern derived from the single-crystal structure.

3.1.2. Hirshfeld surface. We used the Crystal Explorer, which utilizes CIF format files as input for structural data, to investigate the contributions of various types of interactions within the crystal structure because of the intermolecular interactions in the title structure.

Hirshfeld surfaces are generated by dividing the space within a crystal and are visualized using the normalized contact distance, d_{norm}, which is calculated based on the van der Waals

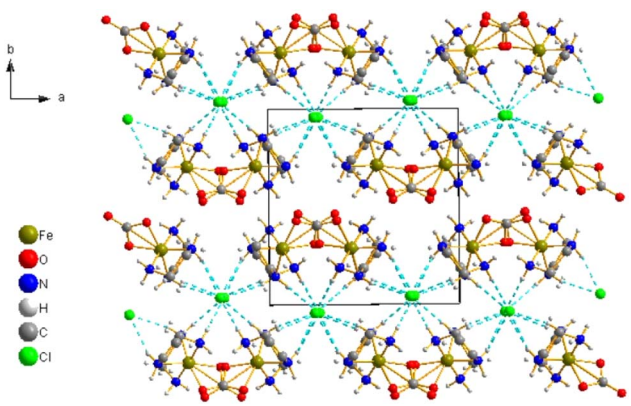

Fig. 3 Projection of the extended lattice along the *c*-axis, highlighting hydrogen-bonding interactions.

Table 3 Intermolecular hydrogen bonds (Å, °) with the symmetry codes[a] in the title compound

D—H···A	d(D—H) (Å)	d(H···A) (Å)	d(D···A) (Å)	(D—H···A) (°)
N1–H1a···Cl1	0.91	2.47	3.343 (2)	161
N1–H1b···O3^{i}	0.91	1.97	2.839 (3)	160
N2–H2a···O2^{ii}	0.91	2.05	2.919 (3)	158
N2–H2b···Cl1^{iii}	0.91	2.41	3.311 (2)	170
N3–H3a···O3^{iv}	0.91	2.27	3.080 (3)	148
N3–H3b···O3^{i}	0.91	2.10	2.955 (3)	156
N4–H4a···Cl1	0.91	2.38	3.274 (2)	167
N4–H4b···Cl1^{iii}	0.91	2.53	3.382 (2)	157
C2–H2d···Cl1^{v}	0.99	2.86	3.681 (3)	141
C3–H3d···Cl1^{vi}	0.99	2.94	3.669 (3)	131
C4–H4d···O1^{vii}	0.99	2.63	3.232 (4)	119
C5–H5b···Cl1^{viii}	0.99	2.84	3.751 (3)	153

[a] Symmetry codes: (i) $x-1/2, -y+1, z$; (ii) $-x+3/2, y, z+1/2$; (iii) $x+1/2, -y+2, z$; (iv) $-x+3/2, y, z-1/2$; (v) $-x+1/2, y, z+1/2$; (vi) $-x+1, -y+2, z+1/2$; (vii) $-x+1, -y+1, z-1/2$; (viii) $-x+1/2, y, z-1/2$.

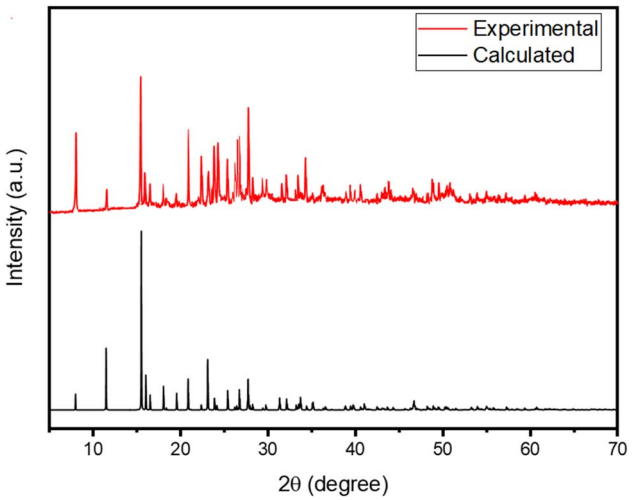

Fig. 4 Room temperature experimental and calculated X-ray diffraction pattern of $[Fe(CO_3)(en)_2]Cl$ crystal sample.

(vdW) radii of atoms as well as the external (d_e) and internal (d_i) distances.

$$d_{norm} = (d_i - r_i^{vdW})/r_i^{vdW} + (d_e - r_e)/r_e^{vdW}$$

where: r_i^{vdW} and r_e^{vdW} represent the van der Waals radii of the atoms located inside and outside the surface, respectively.[61,62] The color scheme of red, white, and blue was used to map d_{norm} onto graphic plots of the Hirshfeld surface. In this scheme, contacts near the van der Waals separation are colored white, longer connections are shown in blue, while shorter ones are shown in red. Additionally, the local curvature of the Hirshfeld surface allows for the visualization of two color-coded properties: the shape index and curvedness.[63]

Intermolecular interactions within the asymmetric unit were analyzed using three-dimensional Hirshfeld surfaces and two-dimensional fingerprint plots. The d_{norm}-colored, intense red-hot areas on the surface are a sign of hydrogen bonding between the nitrogen and oxygen atoms of nearby molecules. The distances to the nearest atoms inside (d_i) and outside (d_e) the Hirshfeld surface are used to identify various intermolecular interactions, as indicated by distinct spots on the surface. As shown in Fig. 5, the overlapping contributions of different types of intermolecular interactions in the full fingerprint are subsequently categorized. The two-dimensional fingerprint plots are presented using d_e and d_i as the axis scales, with a magnified view ranging from 0.6 to 2.4 Å to highlight specific interaction features. The O···H contacts in the title molecular structure are the most frequently occurring interactions globally, accounting for 47.8% of the total HS area on the molecular surface. The fingerprint plot's deconstruction reveals that intermolecular interactions between H···Cl/Cl···H occur as a spike heading toward the lower left of the plot, accounting for 12% of all interactions. With a surface area of 0.8%, O···O is thought to be the third most prevalent intermolecular interaction. The remaining ratios consist of C···H (0.7%) and the C···O contact, which occupies 0.1% of the entire surface, ensuring the lowest proportion.

3.2. Vibrational spectroscopic analysis

To shed additional light on the crystal structure, vibrational characteristics were shown using infrared absorption (Fig. 6).

The fundamental vibrations carried in this spectrum within the following frequency ranges: 3400–2800 cm^{-1} is attributed to the NH_2 and CH_2 stretching modes. The asymmetric stretching

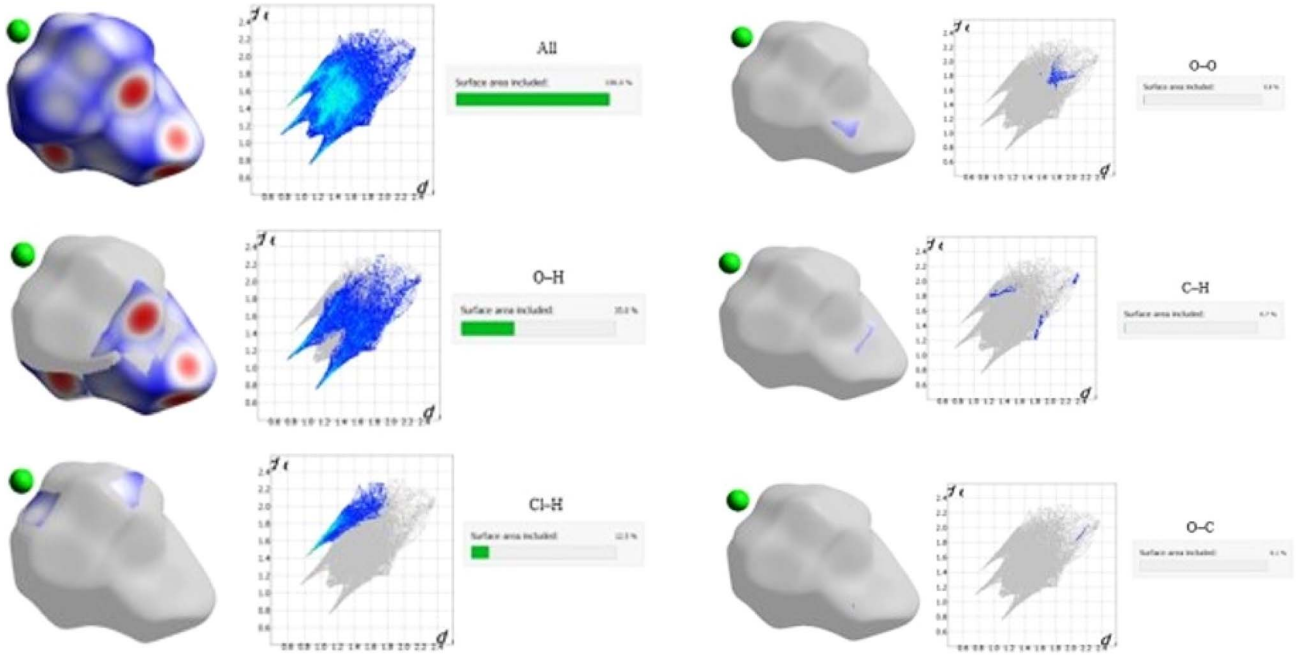

Fig. 5 The two-dimensional fingerprint plot of compound 1 highlights the contributions from various intermolecular contacts.

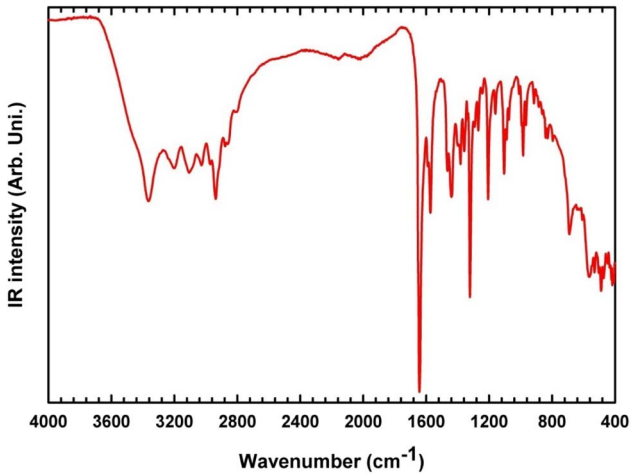

Fig. 6 Infrared spectrum of compound 1.

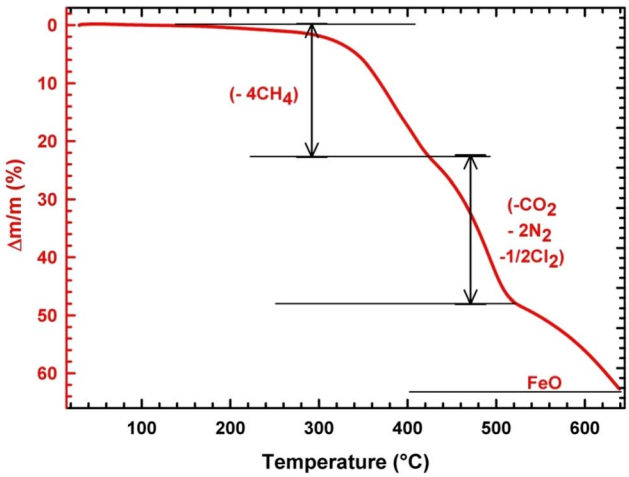

Fig. 8 Thermogravimetric analysis (TGA) curve showing the decomposition of compound 1.

of CH_2 is detected at 2925 cm^{-1}, whereas the symmetric stretching mode is picked up at 2865 cm^{-1}. The checkup of the 1700–450 cm^{-1} range gives the appearance of the bands at 1640 cm^{-1}, which is relative to C=O stretching; at 1485–1445 cm^{-1}, which is ascribed to the CH_2 deformation in-plane. The C–C stretching mode has been assigned to 1092–1103 cm^{-1} and 984 cm^{-1} band. Finally, the bands detected in the infrared spectra within the 700–420 cm^{-1} range were attributed to metal–nitrogen (M–N) stretching vibrations.

The Raman spectrum is given in Fig. 7. The bands between 92 and 430 cm^{-1} probably correspond to either δ(NFeO) or δ(NFeN) mode. These bands correspond to various stretching and deformation modes of the Fe–N and Fe–O bonds. Specifically, two bands observed at 293 and 393 cm^{-1} are attributed to the ν(Fe–N) stretching mode, whereas the band at 203 cm^{-1} is likely assigned to either δ_{NFeN} or δ_{NFeO} mode. Other bands at 1300–1600 cm^{-1} are relative to δ_{NH2} and δ_{CH2} modes. In a high-frequency region 2500–3500 cm^{-1}, the symmetrical and asymmetrical stretch vibrations of CH_2 and NH_2 groups are picked up. Bands around 2800–3000 cm^{-1} are specific to ν_s (CH_2) and ν_{as} (CH_2) modes detected at 2858 and 2910 cm^{-1}, respectively.

3.3. Thermal analysis

Thermogravimetric analysis (TGA) and differential scanning calorimetry (DSC) were conducted to evaluate the thermal stability of the compound. As shown in Fig. 8, the material remains stable up to 298 °C. Its complete decomposition occurs in three distinct stages: the first weight loss of roughly 22.8% (calcd. 23.56%) appears between 300 and 422 degrees Celsius, in harmony with the appearance of an endothermic peak at 380 °C in the DSC curve (Fig. 9).

This degradation is assigned to the departure of four carbon atoms as a gas release of CH_4. The second stage corresponds to the departure of two molecules of N_2, the remaining carbon atom as CO_2, and 1/2 Cl_2, simultaneously with a whole percentage of 48.11% (Theor. 49.7%). As the degradation

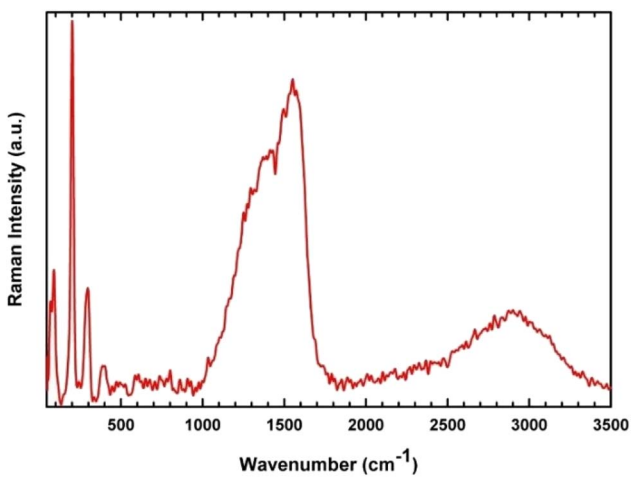

Fig. 7 Raman spectrum of compound 1.

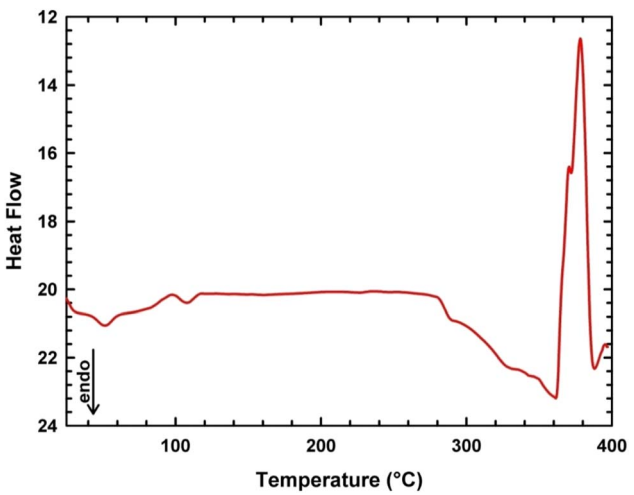

Fig. 9 Thermal analysis curve (DSC) for compound 1.

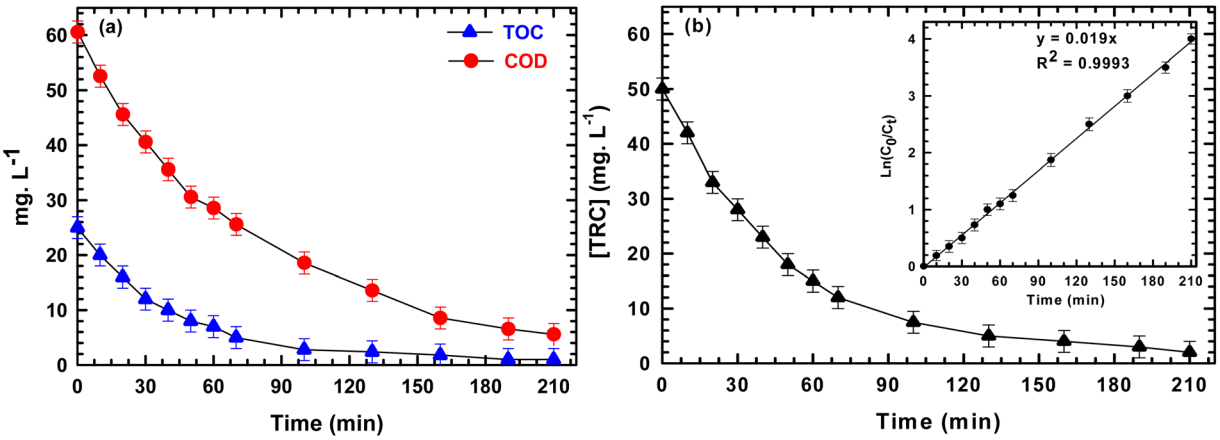

Fig. 10 Mineralization kinetics of triclosan *via* electro-Fenton process with $[Fe(CO_3)(en)_2]Cl$ cathodic modifier. Error bars represent standard deviation of triplicate experiments.

analysis is performed under an O_2 atmosphere, the last stage is relative to the formation of a metal oxide, Fe_2O_3.

3.4. Electro-Fenton performance in triclosan degradation

3.4.1. Kinetics of triclosan degradation. The electro-Fenton process, employing the newly synthesized $[Fe(CO_3)(en)_2]Cl$ complex as a cathodic modifier and a BDD anode, exhibited remarkable efficiency in degrading triclosan. Fig. 10a shows the temporal evolution of both COD and TOC under optimized conditions. A rapid initial decline was recorded within the first 60 minutes, indicating effective oxidative degradation of Triclosan into intermediate organic species. During the early stages, COD removal was notably higher than TOC reduction, suggesting the accumulation of partially oxidized by-products. As electrolysis progressed, the gap between COD and TOC progressively narrowed, reflecting the advanced mineralization of intermediates into CO_2 and H_2O.

After 210 minutes of treatment, mineralization efficiency reached approximately 97% for TOC and 92% for COD, indicating a highly efficient mineralization process. It is worth noting that mineralization efficiency (TOC removal) does not necessarily coincide exactly with the disappearance of the parent compound. While residual traces of triclosan may remain detectable by HPLC, most of the organic carbon is progressively converted into CO_2 and short-chain carboxylic acids during the electro-Fenton process. The slight difference between TCS degradation and TOC removal arises from differences in analytical sensitivity and the transient formation of low-molecular-weight oxidation intermediates. These findings underline the synergistic contribution of rational material design and the high oxidative capability of the electro-Fenton process in treating recalcitrant organic pollutants.[42]. In this context, the behavior of the modified electrode under galvanostatic electro-Fenton conditions provides direct insight into its functional electrochemical activity within the operating system. It is worth emphasizing that the enhanced mineralization performance observed in this system cannot be solely attributed to homogeneous Fenton chemistry. Instead, the results suggest a cooperative mechanism involving both dissolved iron species and interfacial catalytic processes at the modified cathode. The presence of the $[Fe(CO_3)(en)_2]Cl$ complex is expected to modulate the local electrochemical environment, promoting electron transfer and facilitating the Fe^{3+}/Fe^{2+} redox cycle at the electrode interface. Such interfacial effects likely enhance the efficiency of H_2O_2 electrogeneration and improve the overall utilization of reactive oxygen species, thereby contributing to the observed high mineralization rates. This behavior supports the interpretation of the system as a hybrid electro-Fenton process, where homogeneous and interfacial pathways act synergistically rather than independently. To better understand the degradation mechanism, the kinetic behavior of triclosan removal was investigated by modeling the concentration decrease using a pseudo-first-order kinetic approach. The linear graph of $\ln(C_0/C_t)$ plotted against time (Fig. 10b) exhibited an excellent correlation coefficient ($R^2 > 0.99$), indicating that the EF degradation of triclosan follows pseudo-first-order kinetics. The apparent kinetic constant was calculated to be 0.0195 min^{-1}, demonstrating a relatively high reaction rate compared to conventional EF systems reported in the literature.

The elevated k value is ascribed to the increased production of hydroxyl radicals facilitated by the efficient electrochemical reduction of oxygen at the modified cathode and the stable catalytic activity of the iron complex. These kinetic results confirm that the designed hybrid electro-Fenton system not only accelerates the degradation of triclosan but also ensures rapid mineralization of its by-products.[42,43]

3.4.2. Optimization of key electro-Fenton parameters. To determine the optimal operational conditions for triclosan mineralization, the influence of several key parameters including pH, applied current density, and Fe^{2+} concentration was systematically investigated.

3.4.2.1. Effect of pH. The influence of solution pH (2.0–5.0) on Triclosan mineralization was systematically evaluated (Fig. 11). As expected, the electro-Fenton efficiency strongly depended on the acidity of the medium. Maximum TOC

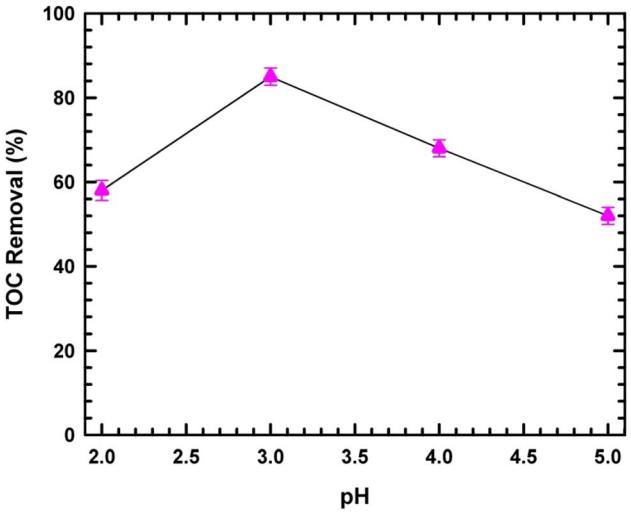

Fig. 11 Effect of initial pH (2.0–5.0) on TOC removal efficiency during electro-Fenton treatment of triclosan (C_0 = 30 mg L^{-1}, [Fe^{2+}] = 0.2 mmol L^{-1}, j = 20 mA cm^{-2}, t = 180 min). Error bars represent standard deviation of triplicate experiments.

removal was achieved at pH 3.0, which is consistent with the optimal pH range reported for homogeneous Fenton systems.

At lower pH values (pH 2.0), the formation of stable iron aqua-complexes reduces the reactivity of Fe^{2+} toward H_2O_2 activation, limiting $^{\bullet}OH$ production. Conversely, at higher pH (≥4.0), partial precipitation of Fe^{3+} as $Fe(OH)_3$ diminishes catalytic redox cycling efficiency. Furthermore, H_2O_2 instability at elevated pH contributes to reduced oxidative performance. Therefore, pH 3.0 was selected as the optimal condition for subsequent experiments.

3.4.2.2. Effect of current density. The applied current density (10–30 mA cm^{-2}) significantly influenced triclosan removal (Fig. 12). Increasing current density from 10 to 20 mA cm^{-2} enhanced mineralization due to increased *in situ* electro-generation of H_2O_2 at the cathode and higher production of anodic hydroxyl radicals at the BDD surface. However, further increase to 30 mA cm^{-2} did not proportionally improve TOC removal, suggesting the onset of parasitic reactions such as oxygen evolution and H_2O_2 decomposition. Excessive current may also promote non-productive radical recombination. Consequently, 20 mA cm^{-2} was identified as the optimal current density, ensuring a balance between radical generation and energy efficiency.

3.4.2.3. Effect of Fe^{2+} concentration. The initial Fe^{2+} concentration (0.1–0.3 mmol L^{-1}) was investigated to determine its impact on catalytic efficiency (Fig. 13). An optimum concentration of 0.2 mmol L^{-1} was observed. At lower Fe^{2+} levels (0.1 mmol L^{-1}), insufficient catalytic activation of H_2O_2 limited $^{\bullet}OH$ generation. In contrast, excessive Fe^{2+} (≥0.3 mmol L^{-1}) resulted in competitive scavenging of hydroxyl radicals according to: $Fe^{2+} + {}^{\bullet}OH \rightarrow Fe^{3+} + OH^-$. This side reaction reduces the effective oxidizing species available for triclosan degradation. Therefore, 0.2 mmol L^{-1} was selected as the optimal concentration to maximize oxidative efficiency while minimizing radical loss.

Overall, the optimization study clearly identifies pH 3.0, 20 mA cm^{-2}, and 0.2 mmol L^{-1} Fe^{2+} as the most favorable operating conditions for triclosan mineralization. These optimization results demonstrate that the enhanced catalytic performance is not solely due to classical Fenton chemistry but also arises from the synergistic interaction between the iron(III) coordination complex and the electrochemical environment, leading to improved Fe^{3+}/Fe^{2+} redox cycling and sustained radical production.

3.4.3. Comparison of triclosan degradation using various advanced oxidation techniques. The degradation efficiency of triclosan was comparatively evaluated using different advanced oxidation processes, including direct anodic oxidation,

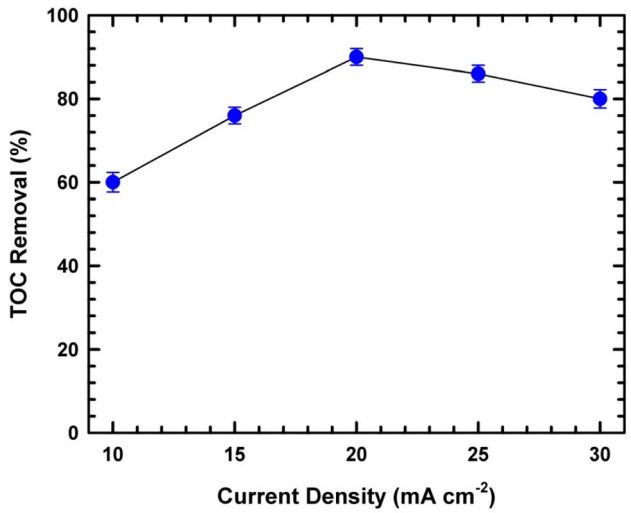

Fig. 12 Influence of applied current density (10–30 mA cm^{-2}) on triclosan mineralization (pH = 3.0, [Fe^{2+}] = 0.2 mmol L^{-1}, t = 180 min). Error bars represent standard deviation of triplicate measurements.

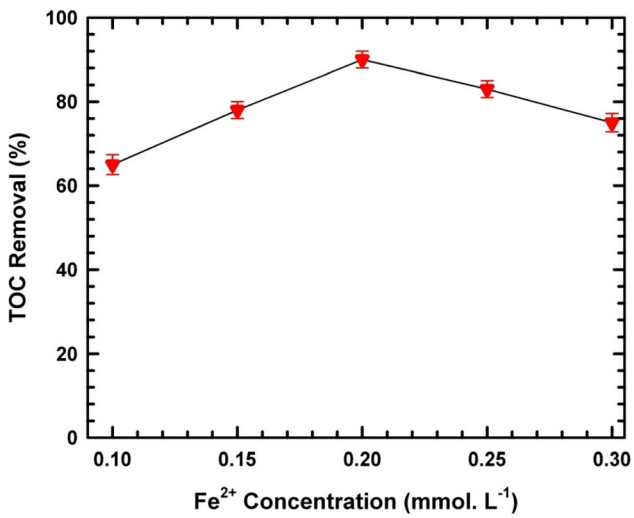

Fig. 13 Effect of initial Fe^{2+} concentration (0.1–0.3 mmol L^{-1}) on TOC removal efficiency (pH = 3.0, j = 20 mA cm^{-2}, t = 180 min). Error bars correspond to standard deviation (n = 3).

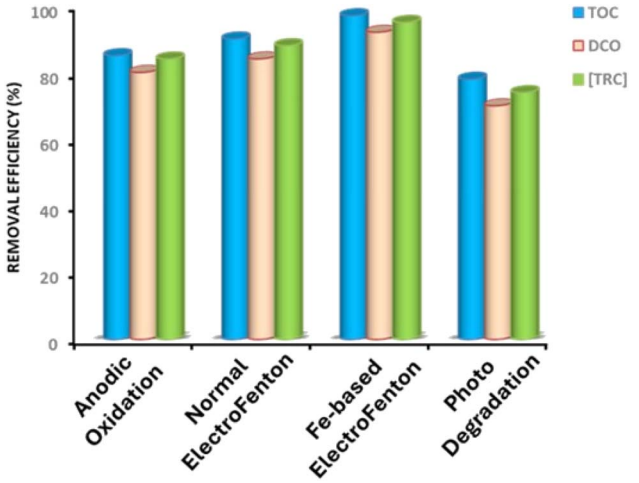

Fig. 14 Comparative efficiency of advanced oxidation processes for triclosan removal.

conventional electro-Fenton with an unmodified cathode, UV photodegradation, and the modified EF system incorporating the synthesized $[Fe(CO_3)(en)_2]Cl$ complex. Fig. 14 presents the removal efficiencies of TOC, COD, and residual triclosan concentration after 180 minutes of treatment under optimized conditions. It should be noted that TOC, COD, and triclosan removal represent different analytical parameters: TOC reflects the degree of mineralization, COD indicates the overall oxidizability of organic species, while triclosan removal corresponds to the degradation of the parent compound. As observed, the modified EF system achieved the highest removal rates, with TOC and COD reductions exceeding 97% and 92%, respectively, alongside nearly complete elimination of triclosan. The apparent differences between these values arise from the formation of intermediate species during the oxidation process, where triclosan is rapidly degraded while mineralization proceeds progressively. In contrast, the unmodified EF system exhibited lower mineralization efficiency, while AO and UV photodegradation resulted in limited degradation and mineralization performance. These findings highlight the catalyst's superior activity and its increased production of hydroxyl radicals in the presence of the iron complex-modified cathode, emphasizing the crucial role of rational electrode design in improving electrochemical water treatment technologies. The enhanced mineralization performance highlights the synergy between efficient radical production and optimized electron transfer pathways afforded by the novel cathodic material.[64]

3.4.4. Identification and evolution of intermediates. Understanding the formation and evolution of intermediate by-products is essential for elucidating the degradation mechanism and assessing the environmental safety of the electro-Fenton process. Monitoring these transient species offers critical insights into the efficiency of the oxidation pathway and the completeness of mineralization. During the electro-Fenton degradation of triclosan using the $[Fe(CO_3)(en)_2]Cl$-modified cathode and BDD anode, several key intermediates were detected and quantified. As shown in Fig. 15a and b, the temporal profiles of aromatic intermediates and short-chain carboxylic acids were characterized by distinct transient behaviors. Aromatic intermediates, including chlorinated phenols and hydroxylated derivatives, exhibited rapid accumulation during the initial 60–90 minutes of electrolysis, corresponding to the active cleavage of the triclosan structure by hydroxyl radicals $^{\bullet}OH$. Among these, 2,4-dichlorophenol and trichlorocatechol were predominant, indicating sequential dechlorination and hydroxylation reactions. Their concentration peaked around 60 minutes, followed by a gradual decline, suggesting further oxidation into non-aromatic compounds. Concurrently, the production of small carboxylic acids like formic, oxalic, and acetic acids became evident. As illustrated, formic acid and acetic acid concentrations increased rapidly,

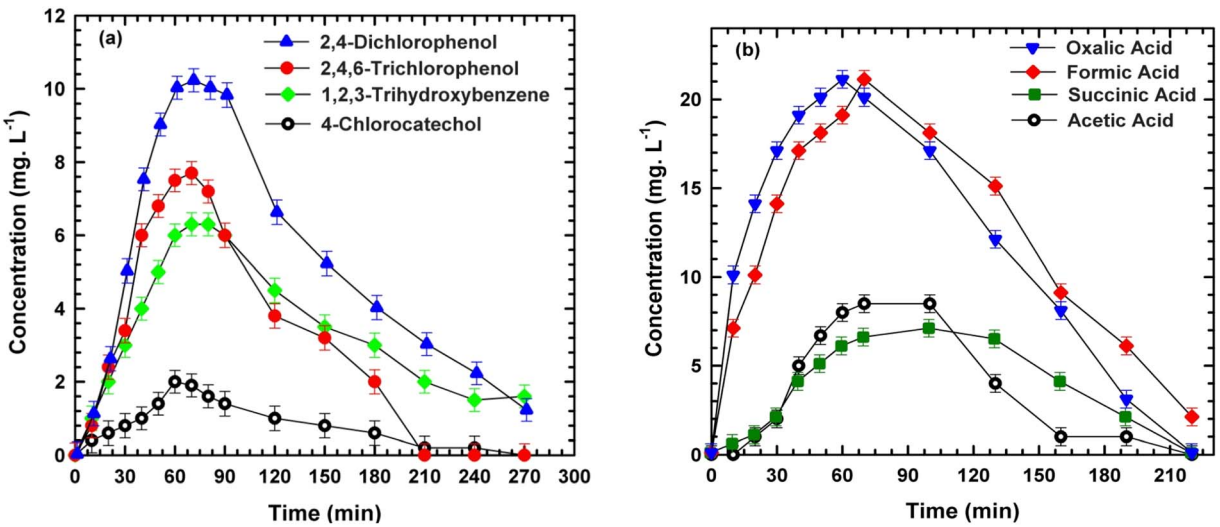

Fig. 15 Time-course profiles of the concentrations of (a) aromatic intermediates and (b) carboxylic acids detected during the electro-Fenton process using a BDD anode and a GCE-modified cathode. Experimental conditions: pH 3.0, initial triclosan concentration $[H_2O_2]_0 = 20$ mM, and initial Fe^{2+} concentration $[Fe^{3+}]_0 = 0.2$ mM. Error bars represent standard deviation of triplicate experiments.

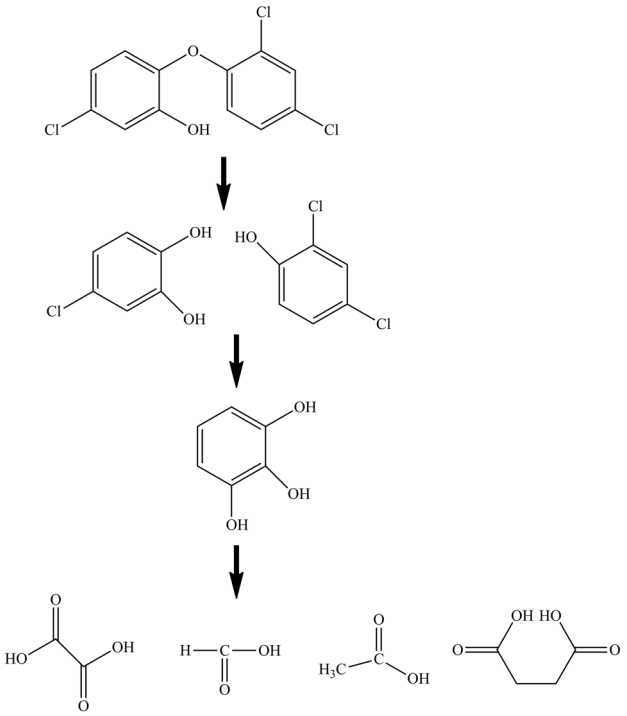

Fig. 16 Proposed pathway for the degradation and mineralization of triclosan in acidic water mediated by hydroxyl radicals generated in the EF process.

reaching maximum levels between 90 and 120 minutes before declining as mineralization advanced. By contrast, oxalic acid exhibited a more persistent profile, accumulating steadily and degrading only slowly during the later stages of treatment. This behavior is consistent with oxalic acid's known resistance to direct hydroxyl radical attack and its role as a final bottleneck in electrochemical mineralization pathways.

3.4.5. Reaction sequence for triclosan degradation. The degradation mechanism of Triclosan under the optimized electro-Fenton system was elucidated by tracking the evolution of organic intermediates, leading to a proposed reaction sequence illustrated in Fig. 16.

The process begins with the electrophilic attack of hydroxyl radicals generated both homogeneously *via* the Fenton reaction and heterogeneously at the surface of the boron-doped diamond anode. These highly reactive radicals target the aromatic rings of the triclosan molecule, initiating hydroxylation and sequential dechlorination reactions. This initial oxidation phase forms several transient intermediates, predominantly chlorinated phenols such as 2,4-dichlorophenol and hydroxylated derivatives like trichlorocatechol, identified based on their characteristic behavior. As oxidation progresses, these aromatic intermediates undergo ring-opening reactions, yielding short-chain aliphatic acids. Notably, formic acid, acetic acid, and oxalic acid were identified and monitored as typical low-molecular-weight carboxylic acids arising from extensive molecular fragmentation. Among the detected acids, formic and acetic acids showed a transient accumulation, reaching peak concentrations between 90 and 120 minutes before gradually declining, indicating ongoing mineralization. In contrast, oxalic acid exhibited a more persistent profile, accumulating steadily and degrading only slowly over time, reflecting its higher resistance to oxidative attack and the need for sustained radical generation in the later stages of the treatment. The proposed reaction pathway highlights the synergistic role of the advanced electrode materials employed: the BDD anode ensures high-efficiency $^{\bullet}OH$ generation and direct oxidation capability, while the $[Fe(CO_3)(en)_2]Cl$-modified cathode facilitates continuous hydrogen peroxide production and efficient Fe^{3+} regeneration, sustaining radical availability throughout the electrolysis. This combined mechanism not only enhances the degradation rate but also promotes near-complete mineralization, providing an efficient and eco-friendly approach for treating triclosan and other persistent organic contaminants.[65]

4 Conclusion

In summary, we have successfully synthesized and thoroughly characterized the novel iron(III) complex $[Fe(CO_3)(en)_2]Cl$, which exhibits a slightly distorted octahedral geometry and forms a robust supramolecular crystal structure supported by extensive hydrogen bonding. The complex demonstrated exceptional catalytic activity as a cathodic modifier in a boron-doped diamond (BDD) electro-Fenton system for the efficient degradation of triclosan. Kinetic studies revealed rapid triclosan mineralization following pseudo-first-order kinetics, with nearly complete removal of organic carbon and chemical oxygen demand after 210 minutes. Comparative analysis confirmed the superior performance of this modified electro-Fenton process over conventional oxidation methods, attributable to enhanced hydroxyl radical generation and effective electron transfer facilitated by the iron complex. Mechanistic insights identified key aromatic and aliphatic intermediates, elucidating a comprehensive degradation pathway culminating in the mineralization of triclosan to CO_2 and H_2O. These results underscore the critical synergy between tailored coordination complexes and advanced electrode materials, paving the way for developing sustainable and high-performance catalytic systems for water purification. The $[Fe(CO_3)(en)_2]Cl$ complex represents a promising candidate for scalable environmental remediation technologies targeting persistent organic pollutants. So, the strong photocatalytic potential of this material under controlled conditions suggests promising applicability in real wastewater treatment. Future studies are expected to demonstrate its robustness in complex effluent matrices, with particular attention to transformation products, toxicity reduction, and long-term stability.

Author contributions

Nejmeddine Rabaaoui: formal analysis, writing – Original draft; Ahlem Guesmi: data curation, methodology; Wiem Jabeur: investigation, validation; Noureddine Mhadhbi: formal analysis, visualization; Nouefel Ben Hamadi: data curation, resources; Lotfi Khezami: data curation, investigation; Mourad

Cherif: conceptualization, investigation, Houcine Naïli: validation, supervision.

Conflicts of interest

The authors declare that they have no known competing financial interests or personal relationships that could have appeared to influence the work reported in this paper.

Data availability

CCDC 2446786 for $[Fe(CO_3)(en)_2]Cl$ contains the supplementary crystallographic data for this paper.[66]

Funding

This work was supported and funded by the Deanship of Scientific Research at Imam Mohammad Ibn Saud Islamic University (IMSIU) (grant number IMSIU-DDRSP2603).

References

1 H. Tllili, S. Walha, S. Elleuch, B. F. Ali and H. Naïli, Structural, vibrational, DFT and optical studies of a new non-centrosymmetric hybrid material $(C_4H_{12}N_2)_{[CoBr4]}$, *J. Mol. Struct.*, 2018, **1152**, 303–310, DOI: 10.1016/j.molstruc.2017.09.096.

2 N. Mhadhbi, S. Saïd, S. Elleuch, T. Lis and H. Naïli, Experimental and DFT characterization of the organic–inorganic monohydrated Co(II) complex with 2,6-diaminopyridine ligand, $(C_5H_8N_3)_2[CoBr_4]\cdot H_2O$, *J. Mol. Struct.*, 2016, **1105**, 16–24, DOI: 10.1016/j.molstruc.2015.10.025.

3 R. Msalmi, S. Elleuch, B. Hamdi, R. Zouari and H. Naïli, Synthesis, DFT calculations, intermolecular interactions and third order nonlinear optical properties of new organoammonium tetrabromocadmate (II): $(C_5H_6N_2Cl)_2[CdBr_4]\cdot H_2O$, *J. Mol. Struct.*, 2020, **1222**, 128853, DOI: 10.1016/j.molstruc.2020.128853.

4 I. Hamdi, Y. Khan, F. Aouaini, J. H. Seo, H.-J. Koo, M. M. Turnbull, B. Walker and H. Naïli, A copper-based 2D hybrid perovskite solar absorber as a potential eco-friendly alternative to lead halide perovskites, *J. Mater. Chem. C*, 2022, **10**, 3738–3745, DOI: 10.1039/D1TC05047H.

5 M. Abid Derbel, M. M. Turnbull, H. Naïli and W. Rekik, A new mixed halide 2D hybrid perovskite: Structural, thermal, optic and magnetic properties, *Polyhedron*, 2019, **175**, 114220, DOI: 10.1016/j.poly.2019.114220.

6 A. M. Ben Salah, N. Sayari, H. Naïli and A. J. Norquist, Chiral and achiral copper(ii) complexes: structure, bonding and biological activities, *RSC Adv.*, 2016, **6**, 59055–59065, DOI: 10.1039/C6RA09630A.

7 N. L. Nkhili, W. Rekik, T. Mhiri, K. T. Mahmudov, M. N. Kopylovich and H. Naïli, ouble piperazinediium and 1,4-diazabicyclo[2.2.2]octanediium M^{II} selenates (M^{II} = Co^{II}, Ni^{II}, Cu^{II}, Zn^{II}) as effective catalysts for Henry reaction, *Inorg. Chim. Acta*, 2014, **412**, 27–31, DOI: 10.1016/j.ica.2013.12.007.

8 W. Rekik, H. Naïli, T. Mhiri and T. Bataille, A new dabco templated metal sulfate, $(C_6H_{14}N_2)[Mn(H_2O)_6](SO_4)_2$. Chemical preparation, hydrogen-bonded structure and thermal decomposition, *J. Chem. Crystallogr.*, 2007, **37**, 147–155, DOI: 10.1007/s10870-006-9170-9.

9 B. M. Hockin, C. Li, N. Robertson and E. Zysman-Colman, Photoredox catalysts based on earth-abundant metal complexes, *Catal. Sci. Technol.*, 2019, **9**, 889–915, DOI: 10.1039/c8cy02336k.

10 O. S. Wenger, Photoactive Complexes with Earth-Abundant Metals, *J. Am. Chem. Soc.*, 2018, **140**(42), 13522–13533, DOI: 10.1021/jacs.8b08822.

11 L. Liu, T. Duchanois, T. Etienne, A. Monari, M. Beley, X. Assfeld, S. Haacke and P. C. Gros, A new record excited state 3MLCT lifetime for metalorganic iron(II) complexes, *Phys. Chem. Chem. Phys.*, 2016, **18**(18), 12550–12556, DOI: 10.1039/c6cp01418f.

12 A. Gualandi, M. Marchini, L. Mengozzi, M. Natali, M. Lucarini, P. Ceroni and P. G. Cozzi, Organocatalytic Enantioselective Alkylation of Aldehydes with [Fe(bpy)3]Br2 Catalyst and Visible Light, *ACS Catal.*, 2015, **5**, 5927–5931, DOI: 10.1021/acscatal.5b01573.

13 J. D. Braun, I. B. Lozada, C. Kolodziej, C. Burda, K. M. E. Newman, J. van Lierop, R. L. Davis and D. E. Herbert, Iron(ii) coordination complexes with panchromatic absorption and nanosecond charge-transfer excited state lifetimes, *Nat. Chem.*, 2019, **11**, 1144–1150, DOI: 10.1038/s41557-019-0357-z.

14 A. Hossain, A. Bhattacharyya, and O. Reiser, in. *Copper's Rapid Ascent in Visible-Light Photoredox Catalysis*, American Association for the Advancement of Science, 2019, 364, 6439, DOI: 10.1126/science.aav9713.

15 C. Minozzi, A. Caron, J. C. Grenier-Petel, J. Santandrea and S. K. Collins, Heteroleptic Copper(I)-Based Complexes for Photocatalysis: Combinatorial Assembly, Discovery, and Optimization, *Angew. Chem., Int. Ed.*, 2018, **57**, 5477–5481, DOI: 10.1002/anie.201800144.

16 A. K. Pal, C. Li, G. S. Hanan and E. Zysman-Colman, Blue-Emissive Cobalt(III) Complexes and Their Use in the Photocatalytic Trifluoromethylation of Polycyclic Aromatic Hydrocarbons, *Angew. Chem., Int. Ed.*, 2018, **57**, 8027–8031, DOI: 10.1002/anie.201802532.

17 P. Herr, F. Glaser, L. A. Büldt, C. B. Larsen and O. S. Wenger, Long-Lived, Strongly Emissive, and Highly Reducing Excited States in Mo(0) Complexes with Chelating Isocyanides, *J. Am. Chem. Soc.*, 2019, **141**, 14394–14402, DOI: 10.1021/jacs.9b07373.

18 M. Grübel, I. Bosque, P. J. Altmann, T. Bach and C. R. Hess, Redox and photocatalytic properties of a Ni^{II} complex with a macrocyclic biquinazoline (Mabiq) ligand, *Chem. Sci.*, 2018, **9**, 3313–3317, DOI: 10.1039/c7sc05320g.

19 W. Sattler, L. M. Henling, J. R. Winkler and H. B. Gray, Bespoke photoreductants: Tungsten arylisocyanides, *J. Am. Chem. Soc.*, 2015, **137**, 1198–1205, DOI: 10.1021/ja510973h.

20 K. T. Yeung, W. P. To, C. Sun, G. Cheng, C. Ma, G. S. M. Tong, C. Yang and C. M. Che, Luminescent Tungsten(VI) Complexes: Photophysics and Applicability to Organic Light-Emitting Diodes and Photocatalysis, *Angew. Chem., Int. Ed.*, 2017, **56**, 133–137, DOI: 10.1002/anie.201608240.

21 Y. Zhang, T. S. Lee, J. L. Petersen and C. Milsmann, A Zirconium Photosensitizer with a Long-Lived Excited State: Mechanistic Insight into Photoinduced Single-Electron Transfer, *J. Am. Chem. Soc.*, 2018, **140**, 5934–5947, DOI: 10.1021/jacs.8b00742.

22 R. S. Jack, G. A. Ayoko, M. O. Adebajo and R. L. Frost, A Review of Iron Species for Visible Light Photocatalytic Water Purification, *Environ. Sci. Pollut. Res. Int.*, 2015, **22**(10), 7439–7449, DOI: 10.1007/s11356-015-4346-5.

23 L. H. M. de Groot, A. Ilic, J. Schwarz and K. Wärnmark, Iron Photoredox Catalysis-Past, Present, and Future, *Am. Chem. Soc.*, 2023, **145**(17), 9369–9388, DOI: 10.1021/jacs.3c01000.

24 P. Vijayarengan, S. C. Panchangam, A. Stephen, G. Bernatsha, G. K. Murali, S. S. Loka, S. K. Manoharan, V. Vemula, R. R. Karri and G. Ravindran, Highly efficient visible light active iron oxide-based photocatalysts for both hydrogen production and dye degradation, *Sci. Rep.*, 2024, **14**, 18299, DOI: 10.1038/s41598-024-69413-4.

25 Q.-Q. Tang, B.-X. Wu, X.-W. Huang, *et al.*, Highly selective in-situ generation of $^1O_2$ via electronic structure regulation of single-atom sites in electro-Fenton system, *Appl. Catal. B Environ.*, 2025, 125040, DOI: 10.1016/j.apcatb.2025.125040.

26 L. Tian, X.-Y. Xia, L.-J. Zhou, *et al.*, Enhanced chlorine enrichment via electron-deficient centers of Co(III) for efficient electrochlorination and ammonia removal, *Appl. Catal. B Environ.*, 2024, **340**, 123260, DOI: 10.1016/j.apcatb.2023.123260.

27 Z. Xu, Z. Liu, S. Li, F. Li, P. Gao, S. Wang, Y. Lin, G. Xiong, Z. Li and H. Peng, Degradation of triclosan by peroxydisulfate/peroxomonosulfate binary oxidants activation under thermal conditions: Efficiency and mechanism, *J. Environ. Manage.*, 2024, **354**, 120211, DOI: 10.1016/J.JENVMAN.2024.120211.

28 P. Iovino, S. Chianese, M. Prisciandaro and D. Musmarra, Triclosan photolysis: operating condition study and photo-oxidation pathway, *Chem. Eng. J.*, 2019, **377**, 121045, DOI: 10.1016/J.CEJ.2019.02.132.

29 P. Pan, Y. Gu, T. Li, N. Y. Zhou and Y. Xu, Deciphering the triclosan degradation mechanism in Sphingomonas sp. strain YL-JM2C: Implications for wastewater treatment and marine resources, *J. Hazard. Mater.*, 2024, **478**, 135511, DOI: 10.1016/J.JHAZMAT.2024.135511.

30 M. H. Cui, Q. Zhang, J. J. Ambuchi, L. Y. Liu, L. Chen, S. M. Niu, C. Zhang, H. B. Liu, C. Tie, X. J. Bi, H. Liu and A. J. Wang, Evaluation of the respective contribution of anode and cathode for triclosan degradation in a bioelectrochemical system, *Bioresour. Technol.*, 2023, **382**, 129121, DOI: 10.1016/J.BIORTECH.2023.129121.

31 J. F. Comar, A. B. S. Nakanishi, F. Sato b, A. N. Medina, J. L. Amaral, G. Costa, E. W. S. Caetano and V. N. Freire, The broad-spectrum biocide triclosan trigonal crystal: Experimental and DFT-calculated structural, electronic and optical properties, *J. Mol. Struct.*, 2025, **1322**, 140235, DOI: 10.1016/J.MOLSTRUC.2024.140235.

32 M. H. Cui, L. Chen, Q. Zhang, L. Y. Liu, H. Pan, H. Liu and A. J. Wang, Understanding the effects of sludge characteristics on the biosorption of triclosan, *Sci. Total Environ.*, 2022, **842**, 156665, DOI: 10.1016/J.SCITOTENV.2022.156665.

33 H. Dai, J. Gao, D. Li, Z. Wang and W. Duan, Metagenomics combined with DNA-based stable isotope probing provide comprehensive insights of active triclosan-degrading bacteria in wastewater treatment, *J. Hazard. Mater.*, 2021, **404**, 124192, DOI: 10.1016/J.JHAZMAT.2020.124192.

34 N. Ozaki, T. Tanaka, T. Kindaichi and A. Ohashi, Photodegradation of fragrance materials and triclosan in water: Direct photolysis and photosensitized degradation, *Environ. Technol. Innov.*, 2021, **23**, 101766, DOI: 10.1016/J.ETI.2021.101766.

35 X. Teng, Z. Wang, M. R. Abukhadra, R. Khaled Mahmoud and R. Qu, Promoted electrochemical degradation of triclosan with persulfate on Fe-Ni oxide modified graphite felt cathode, *Sep. Purif. Technol.*, 2024, **344**, 127229, DOI: 10.1016/J.SEPPUR.2024.127229.

36 V. S. Kosera, T. M. Cruz, E. S. Chaves and E. R. L. Tiburtius, Triclosan degradation by heterogeneous photocatalysis using ZnO immobilized in biopolymer as catalyst, *J. Photochem. Photobiol. A-Chem.*, 2017, **344**, 184–191, DOI: 10.1016/J.JPHOTOCHEM.2017.05.014.

37 A. Batool, S. Shao, K. C. Majhi, A. Mushtaq, Y. Jiang, W. Ho, Y. F. Tsang, Y. He, K. M. Y. Leung and J. C. H. Lam, MnO_2-Catalyzed electrocatalytic mineralization of triclosan in chlorinated wastewater, *Rev. Environ. Sci. Biotechnol.*, 2025, **25**, 100559, DOI: 10.1016/J.ESE.2025.100559.

38 K. B. Orhon, A. K. Orhon, F. B. Dilek and U. Yetis, Triclosan removal from surface water by ozonation - Kinetics and by-products formation, *J. Environ. Manage.*, 2017, **204**, 327–336, DOI: 10.1016/J.JENVMAN.2017.09.025.

39 J. F. Gao, Z. L. Wu, W. J. Duan and W. Z. Zhang, Simultaneous adsorption and degradation of triclosan by Ginkgo biloba L. stabilized Fe/Co bimetallic nanoparticles, *Sci. Total Environ.*, 2019, **662**, 978–989, DOI: 10.1016/J.SCITOTENV.2019.01.194.

40 H. Dai, J. Gao, S. Wang, D. Li and Z. Wang, The key active degrader, metabolic pathway and microbial ecology of triclosan biodegradation in an anoxic/oxic system, *Bioresour. Technol.*, 2020, **317**, 124014, DOI: 10.1016/J.BIORTECH.2020.124014.

41 R. Dhawle, A. Kajtazi, M. Sakellariou, Z. Frontistis, F. Lynen and D. Mantzavinos, Electrochemical oxidation of losartan on a BDD electrode: Influence of cathodes and electrolytes on the degradation kinetics and pathways, *Water Resour. Ind.*, 2024, **31**, 100240, DOI: 10.1016/J.WRI.2024.100240.

42 M. Alizadeh Fard and B. Barkdoll, Effects of oxalate and persulfate addition to Electrofenton and Electrofenton-Fenton processes for oxidation of Ketoprofen: Determination of reactive species and mass balance analysis, *Electrochim. Acta*, 2018, **265**, 209–220, DOI: 10.1016/J.ELECTACTA.2018.01.153.

43 N. K. Saravanakumar and K. N. Palani, Removal of pollutants from pharmaceutical wastewater through electrofenton membrane bioreactor (EFMBR), *Desalination Water Treat.*, 2024, **320**, 100768, DOI: 10.1016/J.DWT.2024.100768.
44 O. V. Dolomanov, L. J. Bourhis, R. J. Gildea, J. A. K. Howard and H. Puschmann, OLEX2: a complete structure solution, refinement and analysis program, *J. Appl. Crystallogr.*, 2009, **42**, 339–341, DOI: 10.1107/S0021889808042726.
45 G. M. Sheldrick, SHELXT – Integrated Space-Group and Crystal-Structure Determination, *Acta Crystallogr., Sect. A: Found. Adv.*, 2015, **71**, 3–8, DOI: 10.1107/S2053273314026370.
46 G. M. Sheldrick, Crystal structure refinement with SHELXL, *Acta Crystallogr., Sect. C: Struct. Chem.*, 2015, **71**, 3–8, DOI: 10.1107/S2053229614024218.
47 K. Brandenburg, *Diamond, Version 3.2i*, Crystal Impact GbR, Bonn, Germany, 2004.
48 N. Rabaaoui, Y. Moussaoui, M. S. Allagui, B. Ahmed and E. Elaloui, Anodic oxidation of nitrobenzene on BDD electrode: Variable effects and mechanisms of degradation, *Sep. Purif. Technol.*, 2013, **107**, 318–323, DOI: 10.1016/J.SEPPUR.2013.01.047.
49 N. Rabaaoui, M. E. K. Saad, Y. Moussaoui, M. S. Allagui, A. Bedoui and E. Elaloui, Anodic oxidation of o-nitrophenol on BDD electrode: Variable effects and mechanisms of degradation, *J. Hazard. Mater.*, 2013, **250–251**, 447–453, DOI: 10.1016/j.jhazmat.2013.02.027.
50 W. Jabeur, M. Korb, J. S. Al-Otaibi, E. Cizmar, R. Badraoui, V. Zelenak and H. Naïli, Physico-chemical characterizations and biological evaluation of a new semiconducting metal–organic compound based on pyrimidine frameworks, *Inorg. Chem. Commun.*, 2022, **139**, 109279, DOI: 10.1016/j.inoche.2022.109279.
51 W. Hallab, A. Guesmi, N. Mhadhbi, L. Khezami, N. B. Hamadi, J. Erwan, A. Sánchez-Coronilla and H. Naïli, Structural, optical, and theoretical investigations of a 2D copper-based perovskite for optoelectronic applications, *J. Mol. Struct.*, 2026, **1349**, 143583, DOI: 10.1016/j.molstruc.2025.143583.
52 W. Hallab, H. Wahbi, R. Msalmi, N. Mhadhbi, F. Saadi, F. Aouaini, B. Basha, A. Sánchez-Coronilla and H. Naïli, *J. Mater. Sci.: Mater. Electron.*, 2025, **36**, 349, DOI: 10.1007/s10854-025-14385-y.
53 S. Alvarez, Distortion Pathways of Transition Metal Coordination Polyhedra Induced by Chelating Topology, *Chem. Rev.*, 2015, **115**, 13447–13483, DOI: 10.1021/acs.chemrev.5b00537.
54 D. Lacková, I. Ondrejkovičová, Z. Padělková and M. Koman, Syntheses, crystal structures, and IR spectra of isonicotinamide-isonicotinamidium bis(isonicotinamide)-tetrakis(isothiocyanato)ferrate(III) and isonicotinamidium chloride, *J. Coord. Chem.*, 2014, **67**(9), 1652–1663, DOI: 10.1080/00958972.2014.917634.
55 L. Jin, X. Xiao, W. Deng, A. Nashalian, D. He, V. Raveendra, C. Yan, H. Su, X. Chu, T. Yang, W. Li, W. Yang and J. Chen, Manipulating Relative Permittivity for High-Performance Wearable Triboelectric Nanogenerators, *Nano Lett.*, 2020, **20**(9), 6404–6411, DOI: 10.1021/acs.nanolett.0c01987.
56 R. Ruswanto, T. Nofianti, R. Mardianingrum and D. Kesuma, Siswandono, Design, molecular docking, and molecular dynamics of thiourea-iron (III) metal complexes as NUDT5 inhibitors for breast cancer treatment, *Heliyon*, 2022, **8**, e10694, DOI: 10.1016/j.heliyon.2022.e10694.
57 A. Ehnbom, S. K. Ghosh, K. G. Lewisa and J. A. Gladysz, Octahedral Werner complexes with substituted ethylenediamine ligands: a stereochemical primer for a historic series of compounds now emerging as a modern family of catalysts, *Chem. Soc. Rev.*, 2016, **45**, 6799–6811, DOI: 10.1039/C6CS00604C.
58 B. LEE, Classification of Conformational Types of Metal Ethylenediamine tetraacetato Complexes, *Inorg. Chem.*, 1972, **11**, 5, https://2024.sci-hub.st/2739/480402777ca63dfa5eeba7d8e69813d6/lee1972.pdf.
59 E. W. Abel, S. R. Allen and B. Khandelwal, Some transition-metal complexes of 1,3,2-dithiarsolane, *J. Chem. Soc., Dalton Trans.*, 1989, **5**, 885–888, DOI: 10.1039/DT9890000885.
60 A. G. Orpen, L. Brammer, F. H. Allen, O. Kennard, D. G. Watson and R. Taylor, Supplement. Tables of bond lengths determined by X-ray and neutron diffraction. Part 2. Organometallic compounds and co-ordination complexes of the d- and f-block metals, *J. Chem. Soc., Dalton Trans.*, 1989, S1–S83, DOI: 10.1039/DT98900000S1.
61 M. A. Spackman and J. J. McKinnon, Fingerprinting intermolecular interactions in molecular crystals, *CrystEngComm*, 2002, **4**(66), 378–392, DOI: 10.1039/b203191b.
62 J. J. McKinnon, D. Jayatilaka and M. A. Spackman, Towards quantitative analysis of intermolecular interactions with Hirshfeld surfaces, *Chem. Commun.*, 2007, **37**, 3814–3816, DOI: 10.1039/b704980c.
63 J. J. Koenderink and A. J. van Doorn, Surface shape and curvature scales, *Image Vis Comput.*, 1992, **10**(8), 557–564, DOI: 10.1016/0262-8856(92)90076-F.
64 M. E. K. Saad, N. Rabaaoui, E. Elaloui and Y. Moussaoui, Mineralization of p-methylphenol in aqueous medium by anodic oxidation with a boron-doped diamond electrode, *Sep. Purif. Technol.*, 2016, **171**, 157–163, DOI: 10.1016/J.SEPPUR.2016.07.018.
65 A. Ouni, N. Rabaaoui, L. Mechi, N. Enaceur, A. K. D. AlSukaibi, E. M. Azzam, K. M. Alenezi and Y. Moussaoui, Removal of pesticide chlorobenzene by anodic degradation: Variable effects and mechanism, *J. Saudi Chem. Soc.*, 2021, **25**(10), 101326, DOI: 10.1016/J.JSCS.2021.101326.
66 CCDC 2446786: Experimental Crystal Structure Determination, 2026, DOI: 10.5517/ccdc.csd.cc2n42lh.